REGIONAL TRAVEL-TIME AND LOCATION UNCERTAINTY ASSESSMENT ALONG THE TETHYAN MARGIN USING A NEW THREE-DIMENSIONAL *P*-VELOCITY MODEL

Megan P. Flanagan [1], Suzan van der Lee[2], Steven C. Myers [1], Sung-Joon Chang [2], and Michael E. Pasyanos[1]

Lawrence Livermore National Laboratory[1] and Northwestern University[2]

Sponsored by the National Nuclear Security Administration

Award Nos. DE-AC52-07NA27344[1] and DE-FC52-04NA25541[2]
Proposal No. BAA04-40

ABSTRACT

We have completed a new, comprehensive three-dimensional model of *S*-velocity in a broad region extending from the western Mediterranean Sea to the Hindu Kush and encompassing Northern Africa, the Arabian Peninsula, and the Middle East. Our joint inversion is an integration of regional waveform constraints, surface-wave group velocity measurements, teleseismic *P* and *S* arrival times, and receiver functions. The data offer complementary sensitivity to crust and mantle structures and are jointly inverted to image the complexity of this tectonically diverse area.

The *S*-wave model is now converted to a *P*-wave model such that we can compute finite difference travel-times through the new model to evaluate *P*-wave arrival times from 'ground-truth' events. The travel times are well predicted by the Joint model at several stations, and the Joint model outperforms the WENA1.0 model, as measured by a higher variance reduction at stations AJM, CFTV, ELL, FRU, KHO, MFP, NIL, RYD, and SVE. The Joint model seems to predict the *P*-wave times particularly well in the eastern part of the model and over portions of northern Africa.

We now use *P*-wave travel-time correction surfaces with our location algorithm to account for three-dimensional *P*-velocity structure and to improve the location estimates of several GT5 and better events that have been regionally recorded throughout the Middle East and North Africa.

OBJECTIVES

Our primary objective is developing new 3-D *S*- and *P*-velocity models for the Middle East and Mediterranean region, including North Africa, southern Europe, and Arabia that

1) are resolved in aseismic regions,
2) are resolved throughout the upper mantle (to 660 km),
3) resolve laterally varying crustal thickness,
4) contain laterally varying vertical velocity gradients,
5) are simultaneously compatible with multiple data sets,
6) utilize several recent, unique waveform data sets, and
7) include uncertainties of the model parameters.

These features would increase the model's ability to predict and calibrate regional travel times and waveforms, thereby providing improved event locations, focal mechanisms, and other event discriminants.

After completing the *S*-wave model we now convert it to a 3-D *P*-velocity model, using teleseismic *P*-arrival times. We test the *P*-wave model's ability to predict regional *P* travel times and to improve location estimates of small regionally recorded events.

RESEARCH ACCOMPLISHED

The study region is centered around the Africa-Arabia-Eurasia triple junction and extends west to the Africa-Eurasia-North America junction at the Azores, and east to the Arabia-Eurasia-Indian Plate junction. The interaction of these five major tectonic plates with each other and with several microplates within an area of one quarter of the Earth's circumference yields this region rich with tectonic complexity. We plan to capture various renditions of this structurally complicated part of the world in one *S*-velocity model through the joint inversion of several different types of seismic data simultaneously; the new model will refine our understanding of the structure and tectonics in this region of the Earth. The data types we combine are constraints from independent studies on the depth to the Moho, fundamental-mode Rayleigh-wave group velocity measurements, waveform fits of regional *S* and Rayleigh waves, and arrival times of teleseismic *S* and *SKS* waves. We convert the resulting *S*-velocity model to a *P*-velocity model with over 2.9 million teleseismic *P* arrival times. Then, we validate our model by performing travel-time prediction with a dataset of ground truth events.

Regional Waveform Fits

We fit over 5,600 available waveforms from the Lawrence Livermore National Laboratory (LLNL) database and MIDSEA dataset (Marone et al., 2004) which sample the Mediterranean region, North Africa, the Middle East, Pakistan, and Afghanistan using the non-linear inversion procedure employed by partitioned waveform inversion. We utilize events with magnitude larger than 4.0 and seismograms with epicentral distance from 5º to 50º. The great-circle wave paths for these seismograms are shown in Figure 1(a). We have estimated path-averaged *S*-velocity structures for these paths using the same starting *S*-velocity model but a different crustal thickness (in 5-km increments) for each path, based on *a priori* reported estimates (Marone et al., 2004).

Teleseismic *S* and *SKS* Arrival Times

We obtained *S* and *SKS* phase arrival time data from two different sources. Both arrival times are adjusted for topography and Earth's ellipticity before inversion. First, we used high-quality relative arrival times of teleseismic *S* and *SKS* waves (Benoit et al., 2006; Park et al., 2007; Schmid et al., 2004) that are measured on broadband seismograms with use of multi-channel cross-correlation (MCCC; VanDecar and Crosson, 1990). Benoit et al. (2006), Park et al. (2007), and Schmid et al. (2004) used seismograms recorded in the Mediterranean, Ethiopia, and Saudi Arabia, respectively. Moreover, we measured additional relative delay times at Turkey and central Asia. The number of *S* phase relative arrival times is over 5900 with epicentral distance of 30º – 90º and the number of *SKS* phase is over 1400 with distance of 87º – 140º; over 7300 in total. Second, we obtained over 223,000 *S* phase arrival time data from the reprocessed ISC database (Engdahl et al., 1998) from 1964 to 2007. We illustrate location of stations and events for each of the two types of arrival-time data in Figure 1(b).

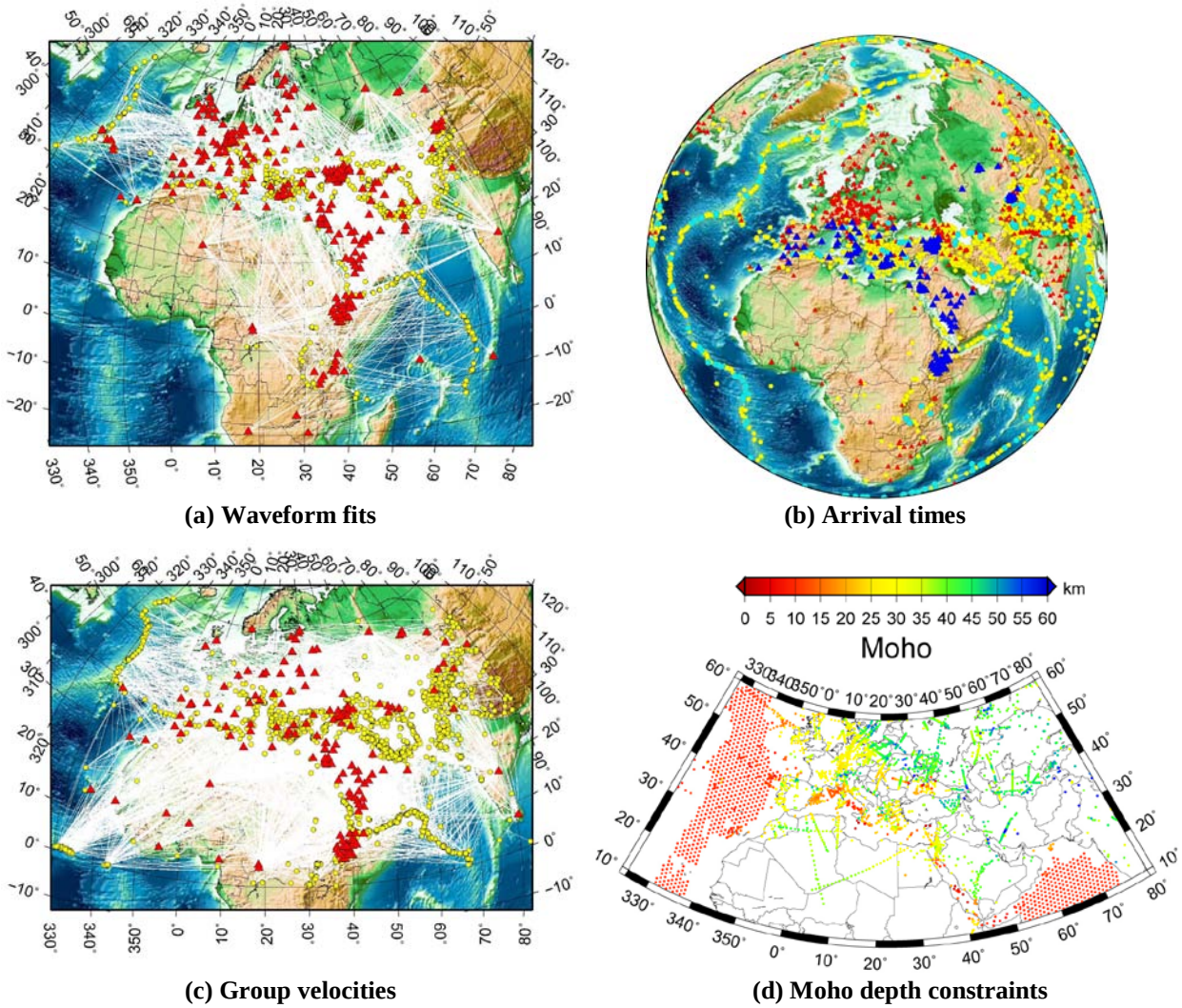

(a) Waveform fits **(b) Arrival times**

(c) Group velocities **(d) Moho depth constraints**

Figure 1. Datasets used for the joint inversion. (a) Ray path coverage for regional waveform fits. Stations are illustrated as red triangles, and events as yellow circles. (b) Events and stations used for teleseismic *S* and *SKS* arrival time estimation. Cyan circles and blue triangles represent events and stations used for relative delay time estimation with MCCC, respectively. Yellow circles and red triangles are events and stations from the reprocessed ISC catalogue. (c) Great-circle wave paths for 45 s period Rayleigh waves. Stations are illustrated as red triangles, and events as yellow circles. (d) Map of the Moho depth distribution acquired from literatures. Artificial point constraints of 10 km depth are placed to the Atlantic and Indian Oceans where measurements are absent.

Surface Wave Group Velocities

We measure over 105,000 group velocities of fundamental-mode Rayleigh waves recorded at MIDSEA and other stations in the region and used them to update previous group velocity maps (Pasyanos, 2005). Figure 1(c) shows the great-circle wave paths for which we included fundamental-mode Rayleigh wave group velocities in our joint inversion. Compared to other data types we include, lateral coverage is best for this group velocity data set, though vertical coverage is provided mainly by the teleseismic arrival times and regional *S* and Rayleigh waveforms. The period for group velocities ranges from 7 to 100 sec.

Crustal Thickness Constraints

While the fundamental-mode Rayleigh-wave group velocities and regional *S* and Rayleigh waveforms have significant sensitivity to Moho depth, they cannot uniquely resolve it. We therefore include independent estimates of crustal thickness as point constraints in the joint inversion and thus compile such measurements from a large number of published studies. A partial list of these studies is provided in Marone et al. (2003) and part of these points stem from the database used for CRUST5.1 (Mooney et al., 2001). We have added new estimates of Moho depth from more recent studies and interactively resolved or removed conflicting data and outliers from the data set. Over 4,700 Moho depth constraints are mapped in Figure 1(d). For the oceans we use a constraint of 10 km for Moho depth, but only for points also covered by data from our other data sets.

Inversion Results

The joint inversion of constraints from regional waveform fits, crustal estimates, group velocities, and teleseismic arrival times produces a new S-wave velocity model shown in Figure 2. The resolving power of the combined data is superior to that of each of the data sets alone. The joint inversion reduces the variance in the data sets by 38% for the teleseismic delay times, 55% for the Rayleigh-wave group velocities, 90% for the Moho point constraints, and 88% for the regional waveform fits. The Moho map, Figure 2a, shows a good resemblance with the point constraints in Figure 1(d), but is much smoother due to the regional waveforms and group velocity data, as well as regularization constraints in the inversion. The map is also broadly consistent with CRUST2.0, except in northern Africa, where the crust from our joint inversion is about 5 km thinner.

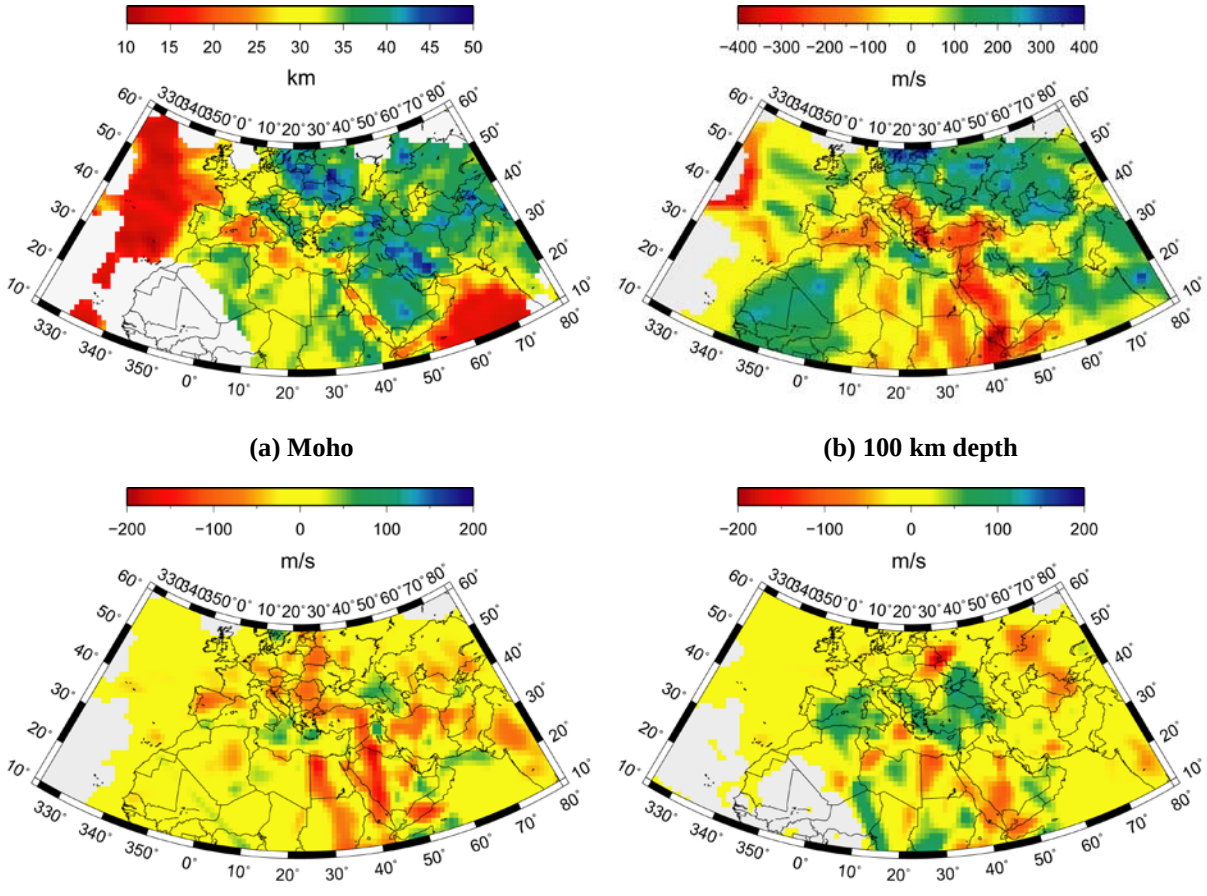

(a) Moho **(b) 100 km depth**

(c) 300 km depth **(d) 500 km depth**

Figure 2. Moho and *S*-wave velocity perturbations resulting from our joint inversion. Moho map (a) and velocity perturbations at 100 km (b), 300 km (c), and 500 km depth (d) are illustrated.

Fast-velocity anomalies are found beneath the West African Craton, the Hellenic trench, the Apennines, the East European Platform, and the Arabian Platform at 75-150 km depth, whereas low-velocity anomalies are located along the plate boundaries such as the mid-Atlantic ridge, Afar, the Anatolian Plateau, Iran, Afghanistan, western Mediterranean Sea, and the Red Sea.

Conversion of *S*-Velocity Model to *P*-Velocity Model

We obtain a *P*-velocity model by performing a *P*-wave arrival time inversion using the equation: $\mathbf{G}_\alpha \mathbf{m}_\alpha = \mathbf{d}_\alpha$, where $\mathbf{G}_\alpha$ is the sensitivity kernel matrix for *P*-wave arrival times, $\mathbf{m}_\alpha$ is the 3-D *P*-velocity model vector, and $\mathbf{d}_\alpha$ is the teleseismic *P*-wave delay vector which is obtained by subtracting predicted arrival times through a reference model from observed arrival times. We use the *S*-velocity model as a preliminary model, because the *S*-velocity model has good resolution for both shallow and deep stucture. We assume that *P*-wave velocity are very close to the *S*-wave velocity anomalies if temperature is the dominant cause of the velocity perturbations based on results in Schmid et al. (2004) in which similarity between *P*- and *S*-velocity anomalies is drawn with use of delay time ratio (see Figure 3a). By multiplication of the *S*-velocity model and *P*-wave sensitivity kernels, we can get predicted *P*-wave delays $\mathbf{d}_{\beta\to\alpha}$ by $\mathbf{m}_\beta$ as in $\mathbf{G}_\alpha \mathbf{m}_\beta = \mathbf{d}_{\beta\to\alpha}$, where $\mathbf{m}_\beta$ is the 3-D *S*-velocity model in m/s scale, and $\mathbf{d}_{\beta\to\alpha}$ is predicted *P* delays by $\mathbf{m}_\beta$. Then, teleseismic *P*-wave delays $\mathbf{d}_\alpha$ can be divided as $\mathbf{d}_\alpha = \mathbf{d}_{\beta\to\alpha} + \mathbf{d}_{res}$, where $\mathbf{d}_{res}$ is the residual *P* delay vector ($\mathbf{d}_\alpha$ and $\mathbf{d}_{\beta\to\alpha}$). Therefore, we have $\mathbf{G}_\alpha(\mathbf{m}_\beta + \mathbf{m}_{new}) = \mathbf{d}_{\beta\to\alpha} + \mathbf{d}_{res}$, which is a linear equation, so we perform the *P*-wave arrival time inversion for $\mathbf{m}_{new}$ using $\mathbf{G}_\alpha \mathbf{m}_{new} = \mathbf{d}_{res}$. A *P*-velocity model is finally obtained by adding $\mathbf{m}_{new}$ to the *S*-velocity model, $\mathbf{m}_\alpha = \mathbf{m}_\beta + \mathbf{m}_{new}$.

The resulting *P*-velocity model with teleseismic *P* arrival time data in Figure 3(b) is shown at various depths in Figure 4. The results are similar to *S*-velocity perturbation results in Figure 2, which means *P*-velocity variations from the *S*-velocity model are small. But higher-velocity anomalies are found in Alps, Hellenides, Turkey, and Hindu Kush than in *S*-velocity model.

Model Evaluation

Distributions of the travel-time residuals with respect to *iasp91* and our joint inversion model (Joint Model) are shown in histogram form in Figure 4 for stations AJM, FRU, KHO, NIL, QUE, PTO, TAM, and TIO. We report both the *L2* norm (variance reduction, VR) and *L1* norm statistics (scaled median absolute deviation reduction, SMADR). The SMAD provides an estimate of the spread of values which is less sensitive to outliers and so is often more appropriate in the presence of non-Gaussian errors.

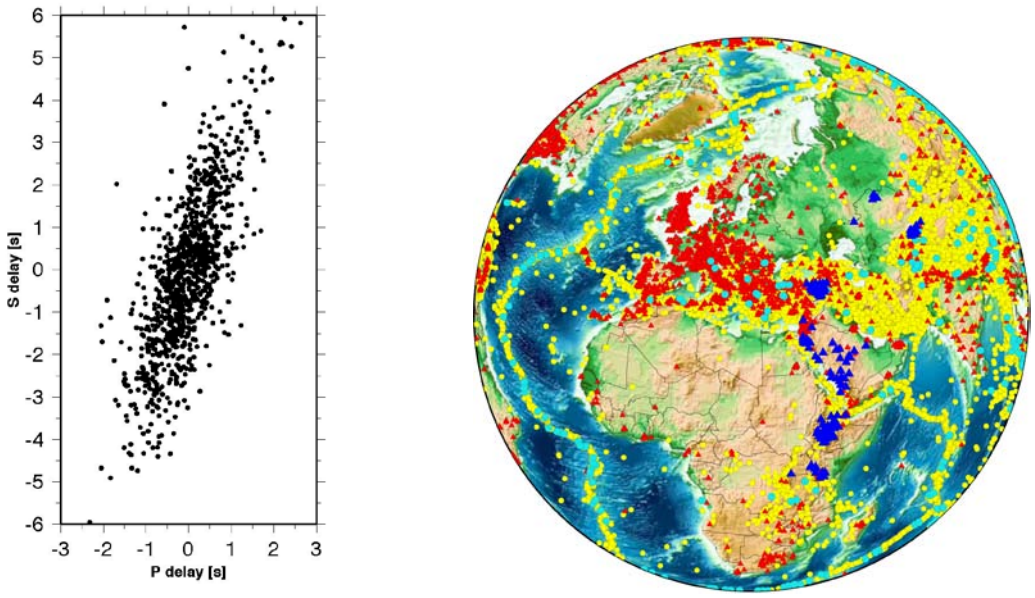

(a) **(b)**

Figure 3. (a) *S* delays versus *P* delays (Schmid et al., 2004). (b) Events and stations used for teleseismic *P* arrival time estimation. Cyan circles and blue triangles represent events and stations used for relative delay time estimation with MCCC, respectively. Yellow circles and red triangles mean events and stations from the reprocessed ISC catalogue.

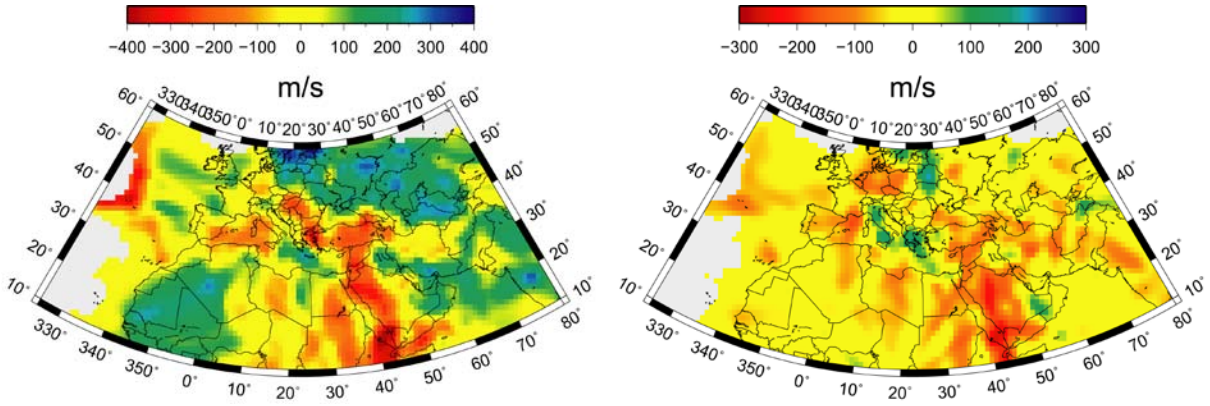

(a) 100 km depth **(b) 200 km depth**

Figure 4. *P*-velocity perturbations at (a) 100 and (b) 200 km depth.

Visually we can evaluate how well the joint inversion model (Joint Model) predicts the data geographically by computing 3D travel-time correction surfaces for some stations. To compute such model-based correction surfaces we subtract the *iasp91*-predicted time from the Joint Model-predicted time using 3D finite-difference algorithm. Example surfaces are shown in Figure 5 for the stations for a source depth of 10 km. Color-coded residuals (data-*iasp91*) from events of focal depth 0 to 20 km are also plotted on top of the surfaces in Figure 5.

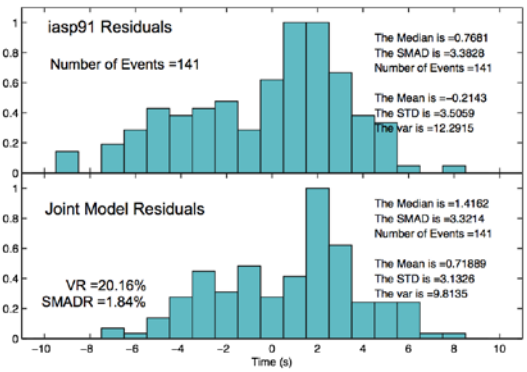

AJM

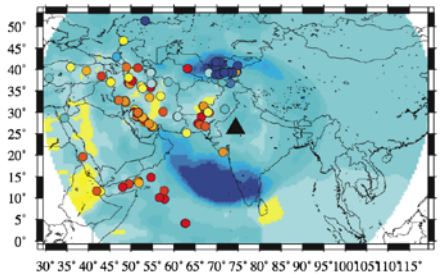

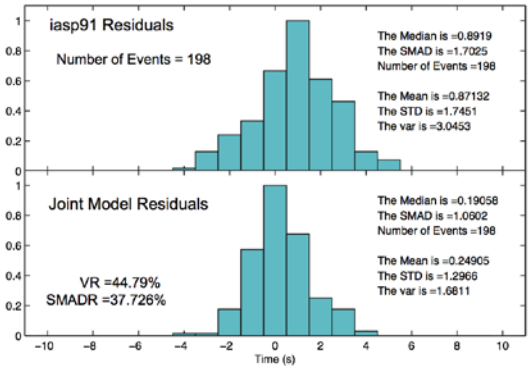

FRU

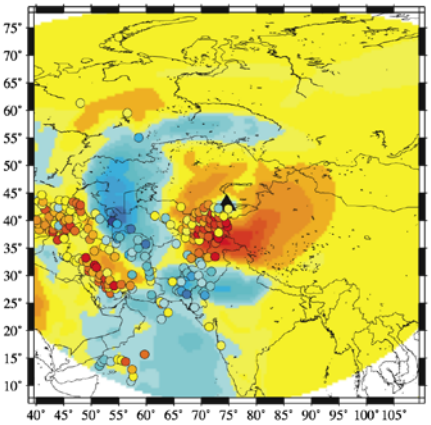

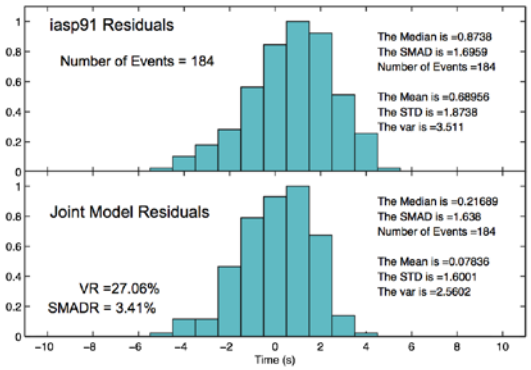

KHO

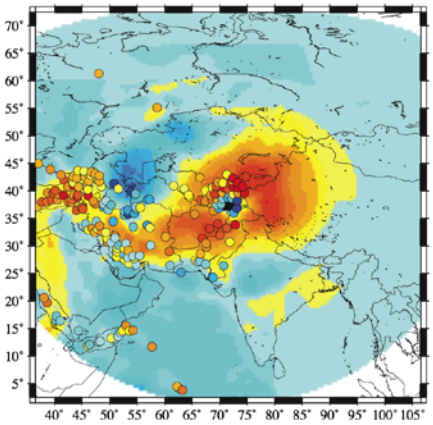

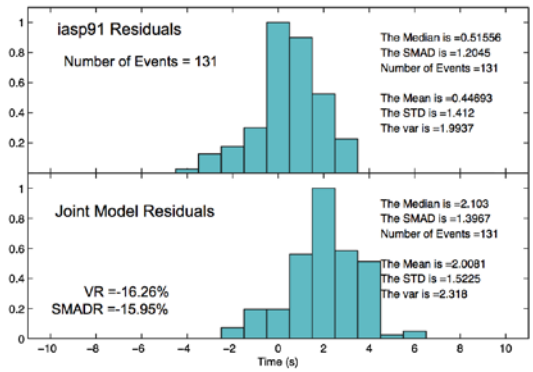

TIO

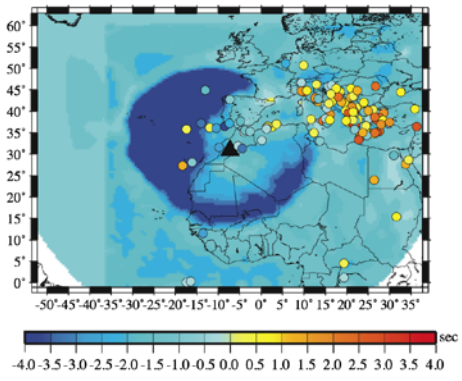

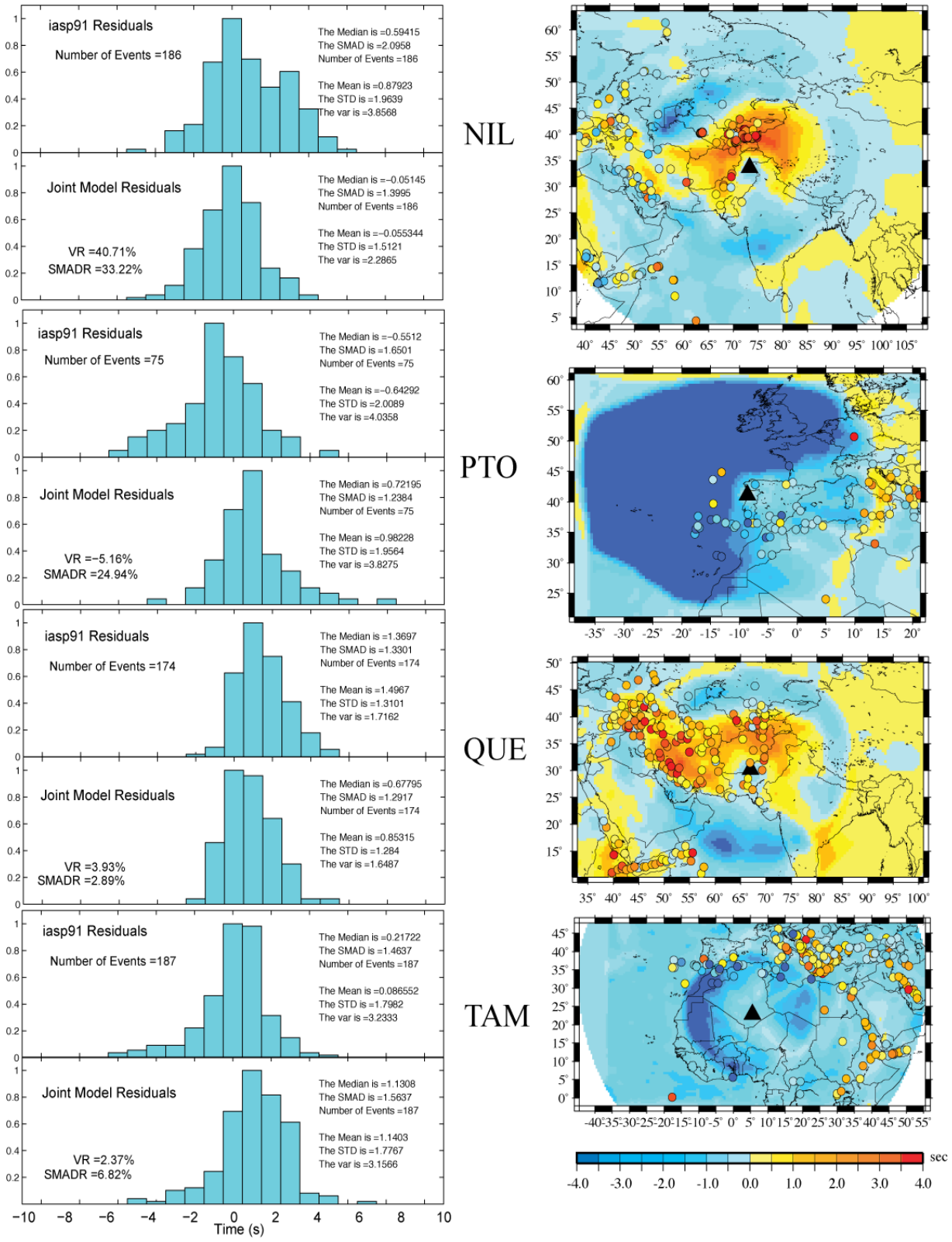

Figure 5. Histograms of *P*-wave travel-time residuals at stations AJM, FRU, KHO, TIO, NIL, PTO, QUE, and TAM along with the travel-time residual surfaces (Joint Model-*iasp91*).

Table 1. Statistics for P wave travel-time fits at each station compared to the WENA1.0 model.

Station	*Ndata*	WENA1.0 *VR*	Joint *VR*	WENA1.0 *smadR*	Joint *smadR*
AJM	141	12.060	20.161	-1.034	1.814
ARO	132	44.909	7.957	35.678	24.158
BGCA	37	-4.77	-7.890	-0.287	32.045
BKR	292	25.314	13.153	14.870	3.468
BRVK	68	32.742	21.539	25.082	12.634
CFTV	10	54.799	66.145	14.631	43.797
DHJN	72	19.160	13.720	-3.590	-20.255
ELL	260	22.270	26.112	6.594	-2.508
FRU	198	9.016	44.797	21.078	37.728
KAD	87	21.216	5.952	15.479	-7.744
KDS	44	51.832	50.409	18.916	17.138
KHO	184	17.485	27.080	4.973	3.419
KUK	35	-5.254	17.443	-14.575	-3.201
LKO	57	27.264	30.827	-11.342	3.912
MAIO	173	33.772	29.848	29.128	26.809
MBO	25	47.220	42.180	37.314	29.343
MFP	9	12.719	29.002	85.685	29.311
MLR	263	-0.201	-10.132	1.164	-16.051
NIL	186	26.998	40.715	19.843	33.224
OBN	341	36.251	18.148	30.332	22.922
PGD	123	-1.178	-7.303	-1.466	-16.850
PTO	75	25.279	5.160	33.897	24.948
QUE	174	-18.418	3.937	-6.033	2.890
RYD	97	1.833	14.488	-0.277	3.557
SHI	180	17.443	31.148	16.935	23.122
SVE	174	21.867	32.319	3.984	4.641
TAB	290	10.398	8.862	5.025	7.714
TAM	187	15.267	2.375	-3.510	-6.829
TCF	246	8.377	-70.257	-18.107	1.473
TIC	100	11.788	9.011	2.813	4.972
TIO	131	10.808	-16.266	-11.024	-15.959
UZH	319	19.898	6.267	-1.958	-0.250
ZGN	104	13.230	9.470	-1.753	-19.406
All data	4814	22.399	22.833	6.205	7.354
GT5 only	146	24.819	26.007	-0.534	6.170

Travel times are well predicted by the Joint model at several stations, and the Joint model outperforms the WENA1.0 model, as measured by a higher *VR*, at many stations. The new Joint model seems to predict the *P* times particularly well in eastern part of the model and over portions of northern Africa.

CONCLUSIONS AND RECOMMENDATIONS

Through a joint inversion of teleseismic *S*-wave arrival time delays, waveform fits of regional *S*- and Rayleigh waves, group velocity measurements of fundamental-mode Rayleigh waves, and independent constraints on Moho depth, we have achieved considerable variance reduction in each data set simultaneously. The new 3-D *S*-velocity model is converted to a *P*-velocity model with teleseismic *P* arrival times and the *P*-velocity model is used for travel-time prediction. Our model generally produces better prediction than *iasp91* 1D model. Our next task is to use travel time correction surfaces with our location algorithm to account for 3D P-velocity structure and improve the location estimates of several GT5 and better events that have been regionally recorded throughout the model area following the techniques of Flanagan et al., 2007.

REFERENCES

Benoit, M. H., A. A. Nyblade, and J. C. VanDecar (2006). Upper mantle *P*-wave speed variations beneath Ethiopia and the origin of the Afar hotspot, *Geology* 34: 329–332.

Engdahl, E.R., R. van der Hilst, and R. Buland (1998). Global teleseismic earthquake relocation with improved travel times and procedures for depth determination, *Bull. Seis. Soc. Am*. 88: 722–743.

Flanagan, M. P., S. C. Myers, and K. D. Koper (2007). Regional travel-time uncertainty and seismic location improvement using 3-dimensional *a priori* velocity models, *Bull Seismol. Soc. Am*. 97: 3, 804–825, *UCRL-JRNL-220179.*

Marone, F. S. Van der Lee, and D. Giardini (2003). Joint inversion of local, regional, and teleseismic data for crustal thickness in the Eurasia-Africa plate boundary region, *Geophys. J. Int*. 154: 499–514.

Marone, F., S. Van der Lee, and D. Giardini (2004). 3-D upper mantle *S*-velocity model for the Eurasia-Africa plate boundary region, *Geophys. J. Int*. 158: 109–130.

Mooney, W., G. Laske, and G. Masters (2001). http://igppweb.ucsd.edu/~gabi/crust.html.

Park, Y., A. A. Nyblade, A. J. Rodgers, and A. Al-Amri (2007). Upper mantle structure beneath the Arabian Peninsula and northern Red Sea from teleseismic body wave tomography: Implication for the origin of Cenozoic uplift and volcanism in the Arabian Shield, *Geochem. Geophys. Geosyst*. 8: Q06021, doi:10.1029/2006GC001566.

Pasyanos, M. E. (2005). A varible-resolution surface wave dispersion study of Eurasia, North Africa, and surrounding regions, *J. Geophys. Res*. 110: B12301, doi:10.1029/2005JB003749.

Schmid, C., S. van der Lee, and D. Giardini (2004). Delay times and shear wave splitting in the Mediterranean region, *Geophys. J. Int*. 159: 275–290.

VanDecar, J.C. and R.S. Crosson (1990). Determination of teleseismic relative phase arrival times using multi-channel cross-correlation and least-squares, *Bull. Seism. Soc. Am*. 80: 150–169.